

Limit Cycle Oscillations in CW Laser Driven NEMS

Keith Aubin, Maxim Zalalutdinov, Tuncay Alan, Robert Reichenbach, Richard Rand,
Alan Zehnder, Jeevak Parpia and Harold Craighead

Abstract—Limit cycle, or self oscillations can occur in a variety of NEMS devices illuminated within an interference field. As the device moves within the field, the quantity of light absorbed and hence the resulting thermal stresses changes, resulting in a feedback loop that can lead to limit cycle oscillations. Examples of devices that exhibit such behavior are discussed as are experimental results demonstrating the onset of limit cycle oscillations as CW laser power is increased. A model describing the motion and heating of the devices is derived and analyzed. Conditions for the onset of limit cycle oscillations are computed as are conditions for these oscillations to be either hysteretic or nonhysteretic. An example simulation of a particular device is discussed and compared with experimental results.

Index Terms—Thermal stress, self-oscillation, limit cycle oscillation, finite element method, laser drive.

I. INTRODUCTION

RESONANT micro and nano-structures have been proposed for a number of applications including sensing, signal processing and as reference oscillators [1], [2], [3], [4]. In sensing applications such as mass detection or strain measurement, the quantity of interest is transduced by frequency change of the oscillator. In a communication system information may be carried by either the frequency or phase. In all these applications drive of the oscillator, signal transduction, attainment of high quality factor and stability are challenges to be met before product can be built.

Self-resonant systems have potential to meet the above challenges. Drive occurs by self-oscillation, the quality factor can be improved through the use of parametric amplification, stability can be improved through the use of feedback and the same optical system used for drive can be used for signal transduction.

A self-resonant system is one that in the absence of external, modulated forcing will vibrate at a steady amplitude, i.e. undergoes limit cycle oscillations. The canonical example is the van der Pol oscillator [5] in which an electrical circuit, containing a vacuum tube that at low current acts as a negative resistor but at high current acts as a positive resistor, spontaneously oscillates.

Thermally driven limit cycle oscillations can occur in mechanical systems at all size scales. For example [6], when solar radiation is incident at an angle upon a space structure,

the absorbed radiation will either increase or decrease as the structure bends toward or away from the incoming radiation. This sets up a feedback loop that can lead either to static bending or to bending vibrations (limit cycle oscillations.)

In micro systems, thermally driven oscillations can occur when a beam or similar structure moves within an interference pattern. Langdon and Dowe [7] demonstrated and analyzed a self-resonant system consisting of an aluminized polyester beam illuminated by a He-Ne laser that passes through a 50% mirror placed just ahead of the polyester beam. The optical arrangement forms a Fabry-Perot interferometer and as the beam vibrates, changing the interferometer gap, the light absorbed by the beam changes, creating a feedback loop between the motion of the beam and the absorbed light. When the laser intensity is low the beam bends statically. As the laser intensity increases, the beam begins to vibrate, i.e. to undergo limit cycle oscillations. Similar results and phenomena were reported by Stokes et al. [8] who demonstrated self-excitation of metal-coated, silicon dioxide beams.

Churenkov [9] analyzed a clamped-clamped beam driven both by externally modulated laser light and by interferometrically modulated light. Conditions for limit cycle oscillations and optimal placement of the light source are analyzed. He notes that parametric excitation due to modulated thermal stresses could be used both in externally modulated and in self-resonant systems. In parametric excitation modulation of the spring stiffness at the right phase and frequency pumps energy into the oscillator, leading to amplification of motion or to unstable oscillations [5]. Churenkov points out that the optimal equilibrium interferometer gap for this mechanism is shifted by $\lambda/8$ compared to the case for excitation due to thermal bending moment and that "self-oscillation cannot be excited spontaneously even if the self-excitation condition is fulfilled."

Hane et al. [10], [11] demonstrated limit cycle oscillations in an aluminum coated, glass cantilevered beam. They demonstrated that the vibration amplitude varied from 0 to 300 nm with a period of $\lambda/2$ as the equilibrium air gap was varied. Zook et al. [12] built a device using an integral photodiode to convert optical power into an electrostatic force to produce self-oscillation in a clamped-clamped silicon microbeam. A proposed application of the device is strain sensing.

Electrostatically driven parametric resonance in MEMS systems has been studied by Turner et al. [13], [14], Ruger and Grütter [15] and Carr et al. [16]. Parametric resonance in an electrostatically driven nanowire was observed by Yu et al. [17]. Ruger and Grütter point out that parametric

drive can be used not only to amplify motion but to reduce thermomechanical noise as well, greatly increasing sensitivity of sensors built using parametric drive.

Zalalutdinov et al. recently produced CW laser driven limit cycle oscillations in NEMS resonators in the shapes of disks [18], domes [19], paddles [20] and wires [21]. Parametric amplification [22], entrainment [23], and operation in air [20] have been demonstrated. These systems were modelled by a one degree of freedom oscillator coupled to a lumped mass thermal system. Up to this time, these models have not been fully analyzed. Thus, in the following sections experimental observations of limit cycle oscillations in three different devices will be presented followed by derivation and analysis of the model and comparison to experimental results from one type of device.

II. EXPERIMENTAL OBSERVATIONS

A. Devices

The devices and fabrication methods used in this study are similar to those used in previous studies [18], [19], [24]. With the exception of the dome oscillator, the devices were made using commercially available silicon-on-insulator (SOI) wafers. Lithography was done using direct write electron beam methods. A chrome etch mask was evaporated onto the surface of the SOI wafer after patterning with lithography. A reactive ion etch (RIE) step removes the top silicon layer after which, the chrome was removed using oxygen plasma. The structures were then released by timing a wet oxide etch in hydrofluoric acid to undercut the oxide from the device.

The devices used were disk, clamped-clamped beam, and dome shaped having resonant frequencies up to 20 MHz (see insets of figures 1, 2, 3). The $21\ \mu\text{m}$ diameter, 250 nm thick disk was made of single crystal silicon supported in the center by an oxide pillar. The wet oxide etch step produced a conically shaped pillar whose lateral dimensions depend on etch time. The oxide thickness is $1\ \mu\text{m}$.

Release of residual stresses during fabrication caused the disks to be arched upwards between 20 and 100 nm at the periphery.

We also fabricated beam oscillators for the purpose of achieving higher frequencies. The device layer in this case was 205 nm thick and the chrome etch mask (50 nm) was left intact.

To create devices with a greater out-of-plane deflection, dome oscillators were fabricated using a different process. First, $1.5\ \mu\text{m}$ of thermal oxide was grown on a [100] silicon wafer. Next, a polycrystalline Si layer was grown using LPCVD ($T = 570^\circ\text{C}$) and annealed at 1150°C for 60 minutes to develop compressive stress ($\approx 300\ \text{MPa}$) in the film. Using photolithography, a hole was patterned and etched through the poly layer using RIE with a resist mask. The device was then released using a wet oxide etch to undercut the patterned hole. As the device layer was freed from the oxide, the compressive stress caused it to buckle, resulting in a $1\ \mu\text{m}$ high, $30\ \mu\text{m}$ diameter dome.

By driving these devices at low amplitude using either a piezo actuator or a modulated laser, a variety of modes can

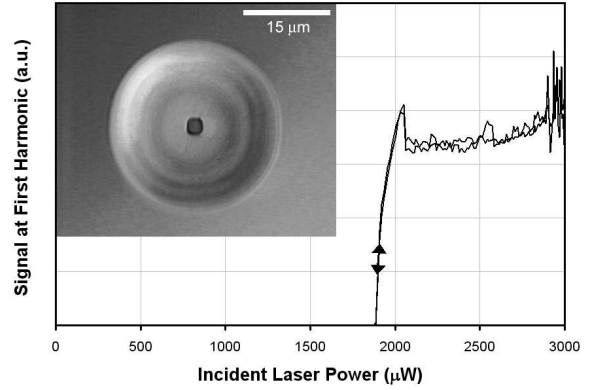


Fig. 1. Dome oscillator (measured frequency = 17.8 MHz, $Q=10,000$) and Hopf bifurcation (onset of self-sustained, or limit cycle, oscillations). Inset is an optical DIC image of the dome. Out-of-plane buckling causes the interference rings seen.

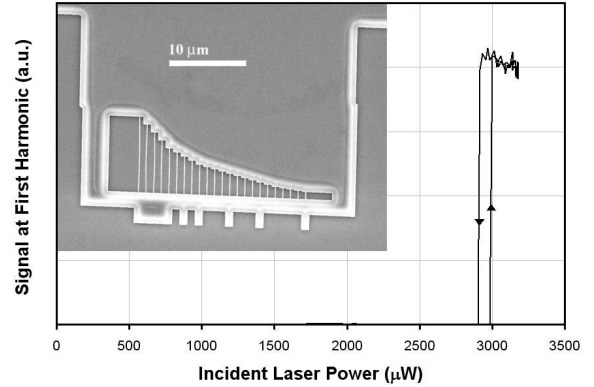


Fig. 2. Hopf bifurcation in doubly clamped beam oscillator (measured frequency=21 MHz). Inset is an SEM image of an array of such resonators. The measured device was the longest beam.

be seen. We have measured modes having zero, one, and two nodal diameters in the disk oscillators as well as higher order modes in the dome oscillators.

B. Setup and Procedures

An interferometric method was used to detect the motion of the devices and has been described in earlier work [25]. A continuous wave (CW) HeNe laser beam is focused to about a $2\ \mu\text{m}$ spot on the device. The layers of device, vacuum, and substrate set up a Fabry-Perot type interferometer whose reflected signal depends on the thickness of the layers. As the device moves, the gap between device and substrate changes and thus modulates the reflected light. This modulated signal is measured using an AC-coupled photodetector and spectrum analyzer. All measurements were done under vacuum (10^{-7} Torr).

The data in figures 1, 2, 3 were taken by measuring the amplitude of the spectral response at the frequency of oscillation of the devices as a function of incident CW laser power using a spectrum analyzer. Changing the DC bias across

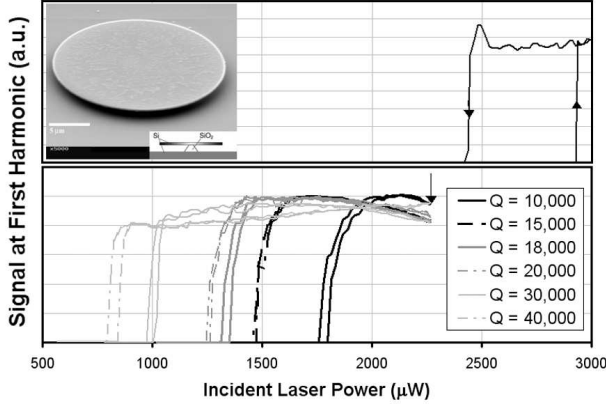


Fig. 3. Hopf bifurcation in two different disk-type oscillators. ($f=3.8$ MHz, $Q=7500$ (top), $f=3.2$ MHz various Q values (bottom)). Inset is a SEM image of the disk. The bottom section shows how the threshold for self-oscillation depends on the quality factor. The arrow shows the point at which the data in figure 4 was taken.

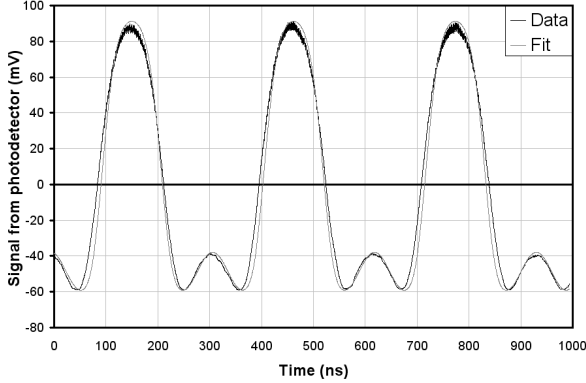


Fig. 4. Signal from photodetector from point indicated by arrow in figure 3. The fit curve is the calculated signal obtained using sinusoidal motion with an amplitude of 80 nm moving through an interference pattern set up by a 248 nm device and 1000 nm gap.

an electro-optical modulator controlled the CW intensity of the laser. Quality factor measurements were taken by driving the structures using a second laser (417 nm) whose intensity was modulated using the RF output from a spectrum analyzer and measuring the half-width of the resonant peak [19]. The CW laser powers were low compared to the power required to induce limit cycle oscillations. In one case, the quality factor of a disk-type oscillator was changed from 10,000 to 40,000 through in-situ laser annealing [26] to measure the threshold power as a function of quality factor. Measurements of the self-oscillation thresholds were taken using laser powers that were below those required to anneal the structure.

C. Results

To produce limit cycle oscillations, we need only to increase the intensity of the CW measurement laser. At a certain power threshold that depends on the device properties and the placement of the beam, the device jumps into motion in

a Hopf-type bifurcation. We estimate that the peak-to-peak amplitude of motion can be as high as half the wavelength of the laser light (315 nm).

Figures 1-3 show the onset of limit cycle oscillations for the different types of structures (domes, beams, and disks) mentioned above. Note that with the detection system used

The amplitude overshoot seen in figures 1 and 3 may be due to temperature dependent reflectivity. Note also that as shown in figure 4 the signal contains significant $2f$ and $3f$ components and hence what is measured is not the true amplitude. To estimate the true amplitude consider the signal from the photodetector while the device is in self-oscillation, as shown in figure 4. The departure from a sinusoidal waveform is due to the $\lambda/2$ periodic dependence of the reflected signal on displacement [27]. We can obtain a rough estimate of the peak-to-peak amplitude of the limit cycle oscillations by fitting to the measured signal a curve produced by mapping sinusoidal motion onto the calculated displacement-reflectance dependence. In figure 4, the amplitude of motion is found to be 160 nm. Amplitudes have been found to be as high as 300 nm.

Various degrees of hysteresis in the amplitude vs. laser power plots of figures 1-3 are observed. For the case of the disk oscillator, one device showed hysteresis while another did not. The two differed in size and in the oxide etch time during fabrication. These differences can cause the devices to have different out-of-plane deflections. This will be shown in the theory section of this paper to have an effect on whether or not hysteresis is expected. The laser power threshold for the onset of limit cycle oscillations was measured for different quality factors in figure 3. The dependence of the laser power threshold, P_{Hopf} on Q is approximately $P_{Hopf} \sim 1/Q^{0.55}$ which differs from the $1/Q$ dependence expected for linear damping, see equation 19 below. It may be that the act of laser annealing the device removes surface contaminants, decreasing surface losses and changing the shape of the disk. This could change the absorption of laser light by the device and hence change the calculated limit cycle threshold.

III. THEORETICAL MODEL

Although the above described systems are structures and hence will have spatially varying fields, for modelling purposes they will be simplified as a one degree of freedom oscillator coupled to a lumped thermal mass. No external forcing is applied to the system.

Let x be the deflection of the structure at the location of laser illumination, and let $z = x/\lambda$, where λ is the wavelength of the laser light. As the structure deforms, the absorption of light will vary periodically with the gap. The absorption can be approximated by $\alpha + \gamma \sin^2 2\pi(z - z_0)$. The values of α and γ depend on the thickness of the structure, the gap and on the optical properties of the material [27], [28]. The position of the minimum of the absorption with respect to the structure's equilibrium position is represented by z_0 .

The structure is assumed to heat up due to absorbed laser light and to cool according to Newton's law of cooling, i.e. the rate of heat loss is proportional to the temperature above

	Si (100) Properties [28], [31]
E	130 GPa
ν	.279
μ	79.1 GPa
ρ	2420 kg/m ³
k	170 W/m K
c	712 J/kg K
a	$2.5 \times 10^{-6}/K$
dE/dT	-130×10^{-4} GPa/K
d μ /dT	-79.1×10^{-4} GPa/K

TABLE I
ROOM TEMPERATURE PROPERTIES OF SI (100)

ambient. Nondimensionalizing time by the small amplitude frequency, ω_0 of the mechanical oscillations, the energy balance for the lumped thermal mass is given by

$$\dot{T} = \frac{1}{\rho c V_{eff} \omega_0} P_{absorbed} - \frac{a_{eff} \bar{h}}{\rho c V_{eff} \omega_0} T \quad (1)$$

where T is the temperature above ambient, ρ is density, c is specific heat, V_{eff} is the effective volume of heated material, a_{eff} is the effective surface area over which cooling occurs, \bar{h} is the cooling coefficient and

$$P_{absorbed} = P \left(\alpha + \gamma \sin^2 2\pi(z - z_0) \right), \quad (2)$$

where P is the incident laser power. The above can be written as

$$\dot{T} + BT = AP \left(\alpha + \gamma \sin^2 2\pi(z - z_0) \right), \quad (3)$$

where $A \equiv \frac{1}{\rho c V_{eff} \omega_0}$ and $B \equiv \frac{a_{eff} \bar{h}}{\rho c V_{eff} \omega_0}$. Expressing the laser power in μW , and T in $^{\circ}C$, A has units of $^{\circ}C/\mu W$, and B is dimensionless. In the above, T represents the maximum temperature in the structure, which occurs at the point of illumination by the laser.

The mechanical system is modelled as a nonlinear, mass-spring-dashpot, coupled to the thermal problem through a thermal forcing and temperature dependent spring stiffness. The temperature dependence of the stiffness has two sources. The elastic properties soften with temperature, see Table I. In-plane thermal stresses may either soften or stiffen the structure. For example, in a doubly clamped beam the relative stiffness change is given by $\frac{\Delta k}{k} = \frac{-12aL^2}{\pi^2 h^2} \Delta T$, where k is the spring stiffness, a is the coefficient of thermal expansion, L is the length of the beam and h is the beam thickness [29]. In the disk oscillator, as the temperature increases, radial tensile and hoop compressive stresses are developed that increase the stiffness of vibration modes involving predominantly radial bending and decrease the stiffness of modes involving predominantly hoop bending [22], [30]. The stiffness change is represented by $\frac{\Delta k}{k} = CT$. C may be positive or negative. At high frequencies, the temperature modulation away from the point of laser heating diminishes, and thus $|C|$ is a decreasing function of frequency of heating modulation.

Opto-thermal forcing can arise from several physical sources, [3], [32], [33], [34]. If there is a through the thickness temperature gradient or if the structure is composed of two layers of different materials, then there will be a thermal bending moment. Fatah [33] discusses deflection of initially

arched beams due to uniform thermal expansion (i.e. no through the thickness thermal gradient.) The electronic strain produced in semiconductors due to photogenerated carriers [35], [36] can be used as a driving mechanism in microbeams [37], [38]. The electronic strain can be many times larger and faster acting than thermal strain, potentially lowering the optical power required for self-oscillation.

The relative importance of the opto-thermal forcing mechanisms depend on the device dimensions, coatings and material. As an example finite element calculations were performed for a 40 μm outer diameter, 6.7 μm inner diameter disk made from 0.24 μm thick, undoped Si, illuminated by a $P = 250 \mu W$ CW laser over a 5 μm diameter circle. Due to the release of residual stresses the disk arches upwards by 40 nm. Since the material is undoped, there will be no electronic strain. Estimating reflectance of 0.35 and absorption of 0.25 [28] the photon force is $F = (2 * 0.35 + 0.25)P/s = 8 \times 10^{-13} N$, where s is the speed of light, resulting in a deflection $\Delta z \approx 0.35 \times 10^{-6} \mu m$. The same illumination will produce $\Delta T \approx 3^{\circ}C$ and $\Delta z \approx 3 \times 10^{-4} \mu m$. Note that if the disk were flat, the only motion would come from the small through-the-thickness temperature gradient. In this case $\Delta z \approx 0.7 \times 10^{-6} \mu m$. To understand why the thermal bending is so small in this case, note that the characteristic time for heat conduction scales as $t = h^2/d$, where $d = k/\rho c$ is the thermal diffusivity. In units of μm and μs , $d = 99 \mu m^2/\mu s$ for Si. The time for the through the thickness temperature to equilibrate is approximately 0.0006 μs . The period of mechanical oscillation for the disk is approximately 1 μs , orders of magnitude longer than the time needed for through the thickness thermal equilibrium.

For the thermal strain driven mechanisms, the static deflection due to the optothermal force can be approximated as DT , where D may be positive or negative and $|D|$ is a decreasing function of heating modulation frequency. In a disk oscillator, supported by a central pillar, if the disk is arched upwards it will deflect down when heated, i.e. $D < 0$. If the disk is arched downward it will deflect up when heated, i.e. $D > 0$. Note that C and D have units of $1/^{\circ}C$.

Putting the above together, the balance of linear momentum for the oscillator may be written in non-dimensional time as

$$\ddot{z} + \frac{1}{Q} (\dot{z} - D\dot{T}) + (1 + CT)(z - DT + \beta(z - DT)^3) = 0 \quad (4)$$

where Q is the quality factor and β the cubic stiffness nonlinearity parameter. Equations 3 and 4 form a coupled system of differential equations describing the vibrations of the NEMS oscillators under CW laser illumination. Note that the DT term could also be considered as a force and placed on the RHS of eq. 4. The results shown in the following sections would be identical to within a very small difference.

To model an actual device, the parameters C , D , A , B , β , z_0 and Q must be estimated. The quality factor Q can be found by mechanically forcing the device and measuring its resonance width. The other parameters can be determined by theory or by computational simulation as outlined in the following sections.

A. Thermal Parameters

For a device that is essentially one-dimensional such as the beam type oscillator, the thermal parameters may be estimated analytically. For a device such as a disk oscillator heated over only a small region, analytical computation of the temperature field is very complex. In such a case the parameters A and B can be determined using two or three dimensional finite element (FEM) simulation. First a static, unit heat flux is applied over the portion of the model illuminated by the laser and the steady state temperature field is computed. The thermal equation then reduces to $BT = A \cdot 1$, and hence $T_{DC} = A/B$, where T_{DC} is the temperature at the location of laser illumination. Next a sinusoidal unit heat flux is applied to the model. In this case the temperature equation reduces to $\dot{T} + BT = A \cdot 1 \sin(\omega\tau)$, where τ is nondimensionalized time, and ω is the frequency of heat flux modulation relative to the natural frequency of vibration of the structure. The steady state solution to the above is $T(\tau) = \frac{A}{\sqrt{B^2 + \omega^2}} \sin(\omega\tau + \delta)$, $\delta = \tan^{-1} -\omega/B$. Hence, T_{AC} , the amplitude of the temperature field from the FEM solution, is $T_{AC} = \frac{A}{\sqrt{B^2 + \omega^2}}$. The parameters A and B can then be found from the solution to the equations for T_{DC} and T_{AC} .

B. Stiffness Change and Cubic Nonlinearity

To determine C , a sinusoidal unit heat flux is applied to a geometrically nonlinear FEM model at or near the resonant frequency of the structure and the temperature and the stress field are computed. After applying enough cycles to reach steady state the simulation is stopped at every $1/8$ period and an eigenmode analysis is performed to extract the resonant frequency of the relevant mode. Since stiffness, $k \sim \omega_0^2$, $\Delta k/k = 2\Delta\omega_0/\omega_0$. By determining the amplitude of the frequency change, $\Delta\omega_0/\omega_0$ over one cycle, $C = \frac{2(\Delta\omega_0/\omega_0)_{AC}}{T_{AC}}$.

The cubic term in the stiffness may be determined by applying a pressure load to the FEM model, performing a nonlinear FEM simulation and fitting the deflection as a function of force. If the amplitude can be measured precisely the cubic term may also be determined by fitting the measured frequency-amplitude curve to the frequency-amplitude relationship for a Duffing oscillator, see ref. [5].

C. Opto-thermal Forcing

The opto-thermal forcing term is modelled in equation 4 as DT . The forcing due to curvature and temperature gradient can be estimated from FEM simulation. Note that if T and z are constant in equation 4, then $z = DT$. Since the NEMS oscillator is a structure, the deflection depends on the temperature field, which differs for static and modulated heating. Thus one needs to find the mechanically static response to a dynamic temperature field. To do this in an FEM simulation, the density can be reduced by a factor (for example) of 10^2 and the specific heat increased by the same factor. This keeps the thermal frequency the same while increasing the mechanical frequency by 10. As before, the procedure now is to apply a modulated unit laser power to the FEM model at or near the

original resonant frequency of the structure. The resulting non-resonant deflection and temperature amplitude are then used to compute $D = \frac{\Delta z}{T_{AC}}$.

IV. ANALYSIS OF MODEL

A. Threshold for Hopf Bifurcation

In this section we present an approximate analytical solution of equations 3, 4 which is based on a few simplifying assumptions. We begin by assuming that $z - z_0$ in eq.(3) is sufficiently small that we can replace $\sin^2 2\pi(z - z_0)$ by the first two terms of its Taylor series:

$$\sin^2 2\pi(z - z_0) \approx 4\pi^2(z - z_0)^2 - \frac{16}{3}\pi^4(z - z_0)^4 \quad (5)$$

Next we assume that the parameters C , D , $1/Q$ and β are small, and we scale them with a single small parameter ϵ . We rescale time to $\tau = \omega t$ and expand $\omega = 1 + \omega_1\epsilon$. These steps result in the following form of the equations:

$$\omega^2 \ddot{z} + \omega \epsilon \frac{1}{Q} (\dot{z} - \epsilon D \dot{T}) + (1 + \epsilon C T)(z - \epsilon D T + \epsilon \beta (z - \epsilon D T)^3) = 0 \quad (6)$$

$$\omega \dot{T} + BT = k_1 + k_2(z - z_0)^2 + k_3(z - z_0)^4 \quad (7)$$

where primes represent differentiation with respect to τ , and where we have defined the quantities $k_1 = AP\alpha$, $k_2 = 4\pi^2 AP\gamma$, $k_3 = -\frac{16}{3}\pi^4 AP\gamma$.

Note that when $\epsilon = 0$ these become:

$$\ddot{z} + z = 0 \quad (8)$$

$$\dot{T} + BT = k_1 + k_2(z - z_0)^2 + k_3(z - z_0)^4 \quad (9)$$

Writing the solution of (8) as

$$z = a \cos \tau + b \sin \tau \quad (10)$$

we obtain a steady state solution to (9) in the form:

$$T = p_1 + p_2 \sin \tau + p_3 \cos \tau + p_4 \sin 2\tau + p_5 \cos 2\tau + p_6 \sin 3\tau + p_7 \cos 3\tau + p_8 \sin 4\tau + p_9 \cos 4\tau \quad (11)$$

where the p_i are known. Substituting (10) and (11) into (6), neglecting terms of $O(\epsilon^2)$, trigonometrically reducing all trig terms in τ , and setting the coefficients of $\sin \tau$ and $\cos \tau$ to zero (for no secular terms) allows us to solve for the coefficients a and b in eq.(10). Switching to polar coordinates

$$a = R \cos \theta \quad \text{and} \quad b = R \sin \theta \quad (12)$$

we are able to obtain an equation on the limit cycle amplitude R , and an expression for the frequency ω_1 in terms of R . The former of these may be written as follows:

$$c_1 R^4 + c_2 R^2 + c_3 = 0 \quad (13)$$

where the coefficients c_i are given by the expressions:

$$\begin{aligned} c_1 &= B^2 C k_3 + C k_3 \\ c_2 &= 6B^2 C k_3 z_0^2 + 6C k_3 z_0^2 + 6B^2 D k_3 z_0 + 24D k_3 z_0 \\ &\quad + B^2 C k_2 + C k_2 \\ c_3 &= 8B^2 D k_3 z_0^3 + 32D k_3 z_0^3 + 4B^2 D k_2 z_0 \\ &\quad + 16D k_2 z_0 - 2B^4/Q - 10B^2/Q - 8/Q \end{aligned}$$

Note that each term of the coefficients c_1 , c_2 and c_3 depends on exactly one of the parameters C , D , $1/Q$, which have been scaled to be $O(\epsilon)$. Thus we may drop the scaling and treat C , D , $1/Q$ in eq.(13) as having their original physical values independent of ϵ .

Eq.(13) can be solved for P :

$$P = \frac{3(B^2 + 1)(B^2 + 4)}{2\pi^2 A Q \gamma K} \quad (14)$$

where

$$K = \lambda_1 R^4 + \lambda_2 R^2 + \lambda_3 \quad (15)$$

$$\lambda_1 = -4\pi^2 (B^2 + 1) C \quad (16)$$

$$\lambda_2 = -24\pi^2 (B^2 + 1) z_0^2 C - 24\pi^2 (B^2 + 4) z_0 D + 3(B^2 + 1) C \quad (17)$$

$$\lambda_3 = -4 (B^2 + 4) D z_0 (8\pi^2 z_0^2 - 3) \quad (18)$$

A Hopf bifurcation in which a limit cycle is born out of $R = 0$ will occur at a value of P which may be obtained by substituting $R = 0$ into eqs.(13)-(18):

$$P_{Hopf} = \frac{3 (B^2 + 1)}{8\pi^2 A D Q z_0 (3 - 8\pi^2 z_0^2) \gamma} \quad (19)$$

To illustrate the results, a standard set of parameter values based on a preliminary analysis of a disk oscillator will be used [23]. These parameters are: $A = 0.018$, $B = 0.488$, $C = 0.000353$, $D = 0.000013$, $\alpha = 0.06$, $\gamma = 0.26$, $\beta = 0.4$, $Q = 10000$, and $z_0 = 0.06$. With these values, equation (19) gives $P_{Hopf} = 474\mu W$.

B. Super and Sub-Critical Hopf Bifurcations

If we use the foregoing parameter values but allow z_0 to vary, eq.(14) gives:

$$P = (-1.02112 z_0^3 - 6.07524 R^2 z_0^2 - 0.76584 R^2 z_0 + 0.0388 z_0 - 1.01254 R^4 + 0.07694 R^2)^{-1} \quad (20)$$

For $z_0 = 0.01$ this gives a subcritical Hopf, whereas for $z_0 = 0.12$ this gives a supercritical Hopf, see Fig.5.

The sub- or super-critical nature of the Hopf will depend on the sign of the curvature (or second derivative) of the curve (14) at $R = 0$:

$$\left. \frac{d^2 P}{dR^2} \right|_{R=0} = \frac{9 (B^2 + 1) G}{16 \pi^2 A (B^2 + 4) D^2 Q z_0^2 (8 \pi^2 z_0^2 - 3)^2 \gamma} \quad (21)$$

where

$$G = 8 \pi^2 B^2 C z_0^2 + 8 \pi^2 C z_0^2 + 8 \pi^2 B^2 D z_0 + 32 \pi^2 D z_0 - B^2 C - C \quad (22)$$

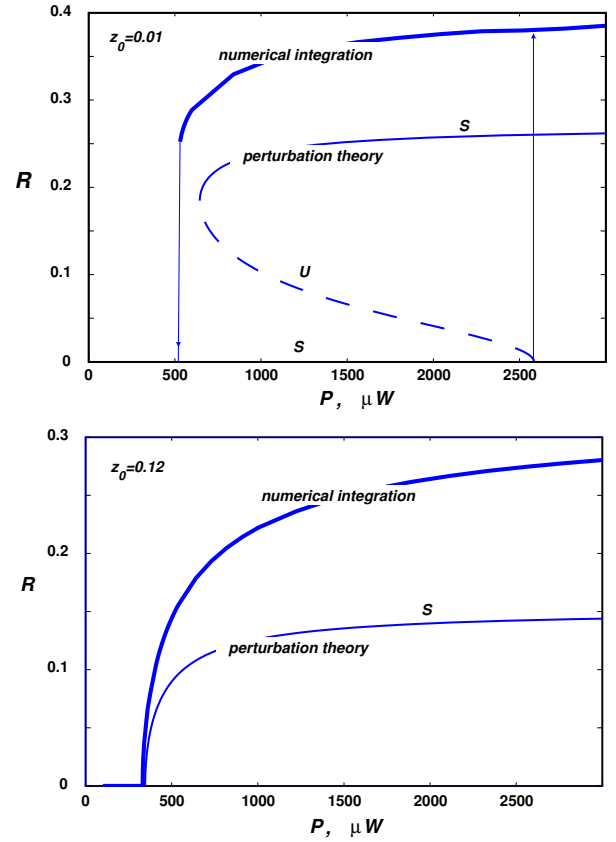


Fig. 5. Subcritical Hopf (upper) versus supercritical Hopf (lower). Amplitude of limit cycle determined from perturbation theory and by numerical integration of equations 3,4. Difference between results is due to Taylor series approximation of $\sin^2 2\pi(z - z_0)$ term. S=stable, U=unstable. Subcritical Hopf involves 0,1 or 2 limit cycles, whereas the supercritical Hopf involves only 0 or 1 limit cycles. In the case of two limit cycles, one is unstable. The stable manifold of the unstable limit cycle separates motions which are attracted to the stable limit cycle from those which are attracted to the equilibrium position. In the case of a subcritical Hopf, the dynamics exhibits hysteresis (represented by vertical lines with arrows showing the direction of jumps), while in the case of a supercritical Hopf no hysteresis occurs. In the case of subcritical Hopf, as Churenkov [9] hints, in the region of 2 limit cycles self-oscillation cannot grow from equilibrium. A sufficiently large initial value of $|z|=R$ must be given to jump from the basin of attraction of the equilibrium point into the basin of attraction of the stable limit cycle.

Note that the sign of $\left. \frac{d^2 P}{dR^2} \right|_{R=0}$ is the sign of G , which therefore determines the nature of the Hopf. For standard parameters, eq.(22) becomes:

$$G = 0.03451 z_0^2 + 0.00435 z_0 - 0.000437065 \quad (23)$$

which has the positive root $z_0 = 0.06596$. Thus the Hopf is supercritical for $z_0 > 0.06596$ and subcritical for $0 < z_0 < 0.06596$.

In general, the cut between sub- and super-critical Hopfs occurs at $G = 0$. For general parameters, we may solve eq.(22) for D , giving the following condition for a supercritical Hopf:

$$D > \frac{(B^2 + 1) C (1 - 8 \pi^2 z_0^2)}{8 \pi^2 (B^2 + 4) z_0} \quad (24)$$

Thus in general the nature of the Hopf will depend on D , C , B and z_0 . However, this equation shows that if $z_0 > 1/(\sqrt{8\pi}) =$

0.112, the RHS of eq.(24) will be negative, and the Hopf will always be supercritical.

Note that eq. 5, the Taylor series approximation of the interference field gives the correct value of P_{Hopf} but not of the limit cycle amplitude, see figure 5, since the approximation is inaccurate for large values of $z - z_0$.

C. Number of Limit Cycles

The system of equations (3),(4) can exhibit 0,1 or 2 limit cycles, depending on the value of the parameters. We have already seen this in Fig.5. In this section we investigate how the number of limit cycles depends on the value of the parameters C and D .

For the standard parameters, eq. (13) becomes

$$CR^4 + (1.232D - 0.0544C)R^2 - 0.0565D + 5.364 \times 10^{-7} = 0 \quad (25)$$

For the standard values of C and D , solving eq. (25) for the single real positive root for R , yields $R = 0.169$, the approximate amplitude of the limit cycle.

For a real solution R to (25), the discriminant ≥ 0 , which requires

$$5813930.0 D^2 + 352252.6 C D + 11326.8 C^2 - 8.21418 C > 0 \quad (26)$$

In addition to being real, the roots $R^2 > 0$. The cut comes when $R = 0$, which happens when

$$D = 9.49 \times 10^{-6} \quad (27)$$

The curve (26) and the line (27) divide the C - D parameter plane into regions which contain 0,1 or 2 limit cycles for fixed values of the other parameters, see Fig.6.

D. Simulation of Single Crystal Si Disk Oscillators

To demonstrate the application of the theory and procedures to an actual device, limit cycle oscillations in a $40\mu\text{m}$ outer diameter, $6.7\mu\text{m}$ inner diameter, 240 nm thick disk on a $1000\mu\text{m}$ thick SiO_2 substrate were simulated. The disk was not completely flat; it was arched upwards with a deflection of approximately 40 nm at its edge. The interference absorption curve can be approximated by $\alpha = 0.05$, $\gamma = 0.25$, $z_0 = -0.09$. Using the finite element method and the properties given in table 1, the thermal parameters are estimated to be $A = 0.006^\circ\text{C}/\mu\text{W}$ $B = .29$. The mechanical parameters are estimated to be $C = 3.1 \times 10^{-4}/^\circ\text{C}$, $D = -4.4 \times 10^{-5}/^\circ\text{C}$, $\beta = 0.4$. The quality factor, $Q \approx 5200$. Using equation 19 $P_{Hopf} = 280\mu\text{W}$ for $Q = 10,000$ and $P_{Hopf} = 540$ for $Q = 5200$. Numerical integration of the model equations shows a supercritical bifurcation. Experiments show a supercritical bifurcation with $P_{Hopf} \approx 250\mu\text{W}$ for $Q = 10,000$ and $P_{Hopf} \approx 300$ for $Q = 5200$.

A similar analysis was performed for a disk with $21\mu\text{m}$ outer diameter, $0.8\mu\text{m}$ inner diameter, 250nm thick, initially arched up by 30nm on the periphery. The resulting

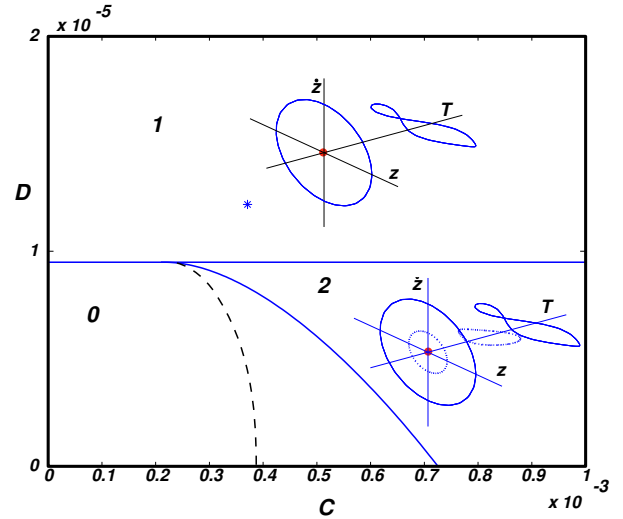


Fig. 6. Number of limit cycles displayed in the C - D parameter plane, for standard parameters at $P = 600\mu\text{W}$. Each region contains a schematic of the limit cycles projected onto the z - \dot{z} and z - T phase planes. In region 0 there are no limit cycles and the origin is stable. In region 1 there is one stable limit cycle and the origin is unstable. In region 2 there are two limit cycles (the larger is stable and the smaller is unstable) and the origin is stable. The * corresponds to the location of the standard parameters. The solid curved line is eq.(26), and the straight line is eq.(27). Numerical integration of eqs.(4),(3) with the approximation (5) agrees well with the solid curved line, eq.(26). Numerical integration of eqs.(4),(3) without the approximation (5) gives the dashed curved line. Eq.(27) agrees with numerical integration results in both cases.

parameters for this model are $A = .0025^\circ\text{C}/\mu\text{W}$, $B = .12$, $C = 5 \times 10^{-4}/^\circ\text{C}$, $D = -.95 \times 10^{-5}/^\circ\text{C}$, $z_0 = -.075$, and $\beta = 0.4$. Using equation 19, $P_{Hopf} = 4490\mu\text{W}$ for $Q = 7500$. The numerical simulations show a subcritical bifurcation, in agreement with the experimental results in figure 3 (top). However the value of P_{Hopf} is larger than that obtained experimentally ($2800\mu\text{W}$ for $Q = 7500$.)

A similar analysis has not been performed for the polysilicon dome or for the single crystal beams. However, the procedure would be the same.

V. SUMMARY AND CONCLUSIONS

Opto-thermally driven limit cycle oscillations can occur in NEMS and MEMS devices that are illuminated within an interference fringe field where the amount of light absorbed is a function of the deflection of the NEMS device. The forces that drive the oscillation can be due to thermal bending, thermal expansion of non-planar devices, thermal strain driven stiffness modulation, photon pressure and opto-electronic strain. These phenomena can be modelled using a system of two coupled, non-linear differential equations 3 and 4, containing 7 parameters that describe the system. Analysis of the model equations provides an expression (eqn. 19) for P_{Hopf} , the CW laser power needed for limit cycle oscillations to occur. The analysis also gives conditions for sub- and supercritical Hopf bifurcations, corresponding physically to cases where the limit cycle oscillations would or would not show hysteresis as the CW laser power is increased and decreased.

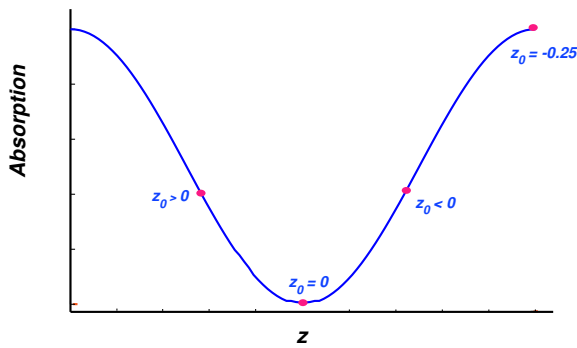


Fig. 7. Schematic absorption versus oscillator deflection (eqn. 2). Dots denote equilibrium positions ($z \approx 0$) for different z_0 values. For $D > 0$ self-oscillation can occur when $z_0 > 0$, i.e. the slope of the absorption curve is negative at the oscillator's equilibrium position. For $D < 0$ self-oscillation can occur when $z_0 < 0$, i.e. slope is positive at the equilibrium position. Parametric pumping term (CT) is most effective for $C > 0$ when $z_0 \approx 0$. If $C < 0$, then CT term is most effective for $z_0 \approx 0.25$.

The relationship between the parameters C (parametric pumping term), D (deflection due to heating term) and z_0 (offset to interference absorption curve) is outlined in Figure 7. Depending on the signs of C and D these terms will be effective either in driving limit cycle oscillations or suppressing them depending on the location of the interference absorption minima and maxima with respect to the equilibrium position of the oscillator.

Predictions of the model equations agree well with experiments, although due to the uncertainty in the many model parameters it is difficult to predict P_{Hopf} exactly. The value of P_{Hopf} and the nature of the bifurcation depends at least linearly on all of the parameters, see eq. 19. These parameters in turn depend on the elastic modulus, optical properties, and thermal properties of the material. For example, if the elastic modulus were doubled, the frequency would of course increase by $\sqrt{2}$, but C , would not change as this parameter describes the *relative* stiffness modulation and hence does not depend on E . However, the thermal parameter B will depend linearly on the thermal conductivity, k , which can depend on device thickness and grain structure.

ACKNOWLEDGMENT

This work was supported by the Cornell Center for Materials Research (CCMR), a Materials Science and Engineering Center of the National Science Foundation (DMR-0079992). This work was performed in part at the Cornell NanoScale Facility (a member of the National Nanotechnology Infrastructure Network) which is supported by the National Science Foundation under Grant ECS-0335765, its users, Cornell University and Industrial Affiliates.

REFERENCES

- [1] J. D. Zook, W. R. Herb, C. J. Bassett, T. Stark, J. N. Schoess, and M. L. Wilson, "Fiber-optic vibration sensor based on frequency modulation of light-excited oscillators," *Sensors and Actuators A*, vol. 83, pp. 270–276, 2000.
- [2] B. Ilic, D. Czaplewski, H. G. Craighead, P. Neuzil, C. Campagnolo, and C. Batt, "Mechanical resonant immunospecific biological detector," *Applied Physics Letters*, vol. 77, pp. 450–452, 2000.
- [3] R. Langdon and B. J. Lynch, "Photoacoustics in optical sensors," *GEC Journal of Research*, vol. 6, pp. 55–62, 1988.
- [4] S. Lee, M. U. Demirci, and C. T. C. Nguyen, "A 10-mhz micromechanical resonator pierce reference oscillator for communications," in *Digest of Technical Papers, the 11th International Conference on Solid-State Sensors and Actuators (Transducers01)*, 2001, pp. 1094–1097.
- [5] R. Rand, *Lecture Notes on Nonlinear Vibrations*. Cornell University, available at <http://www.tam.cornell.edu/randdocs/>, 2003.
- [6] E. A. Thornton, *Thermal Structures for Aerospace Applications*. American Institute of Aeronautics and Astronautics, Inc., 1996.
- [7] R. M. Langdon and D. Dowe, "Photoacoustic oscillator sensors," in *Fiber Optic Sensors II*, A. M. Scheggi, Ed., vol. 798. The Hague, The Netherlands: SPIE, April 1987, pp. 86–93.
- [8] N. A. D. Stokes, R. M. A. Fatah, and S. Venkatesh, "Self-excitation in fibre-optic microresonator sensors," *Sensors and Actuators A*, vol. 21, pp. 369–372, 1990.
- [9] A. V. Churenkov, "Photothermal excitation and self-excitation of silicon microresonators," *Sensors and Actuators A*, vol. 39, pp. 141–148, 1993.
- [10] K. Hane and K. Suzuki, "Self-excited vibration of a self-supporting thin film caused by laser irradiation," *Sensors and Actuators A*, vol. 51, pp. 179–182, 1996.
- [11] K. Hane, "Analytical modeling of micromachined resonator sensor activated by cw laser irradiation," in *Proc. 1997 International Conference on Solid-State Sensors and Actuators (Transducers'97)*, Chicago, June 1997, pp. 105–107.
- [12] J. D. Zook, D. W. Burns, W. R. Herb, H. Guckel, J.-W. Kang, and Y. Ahn, "Optically excited self-resonant microbeams," *Sensors and Actuators A*, vol. 52, pp. 92–98, 1996.
- [13] K. L. Turner, S. A. Miller, P. G. Hartwell, N. C. MacDonald, S. H. Strogatz, and S. g. Adams, "Five parametric resonances in a microelectromechanical system," *Nature*, vol. 396, pp. 149–152, 1998.
- [14] W. Zhang, R. Baskaran, and K. L. Turner, "Effect of cubic nonlinearity on auto-parametrically amplified resonant mems mass sensor," *Sensors and Actuators A*, vol. 102, pp. 139–150, 2002.
- [15] D. Rugar and P. Grütter, "Mechanical parametric amplification and thermomechanical noise squeezing," *Physical Review Letters*, vol. 67, pp. 699–702, 1991.
- [16] D. W. Carr, S. Evoy, L. Sekaric, H. G. Craighead, and J. M. Parpia, "Parametric amplification in a torsional microresonator," *Applied Physics Letters*, vol. 77, pp. 1545–1547, 2000.
- [17] M.-F. Yu, G. J. Wagner, R. S. Ruoff, and M. J. Dyer, "Realization of parametric resonance in a nanowire mechanical system with nanomanipulation inside a scanning electron microscope," *Physical Review B*, vol. 66, pp. 1–4, 2002.
- [18] M. Zalalutdinov, A. T. Zehnder, A. Olkhovets, S. Turner, L. Sekaric, B. Ilic, D. Czaplewski, J. M. Parpia, and H. G. Craighead, "Autoparametric optical drive for micromechanical oscillators," *Applied Physics Letters*, vol. 79, pp. 695–697, 2001.
- [19] M. Zalalutdinov, K. Aubin, C. Michael, R. Reichenbach, T. Alan, A. Zehnder, B. Houston, J. Parpia, and H. Craighead, "Shell-type micromechanical oscillator," in *Microtechnologies for the New Millennium*, 2003.
- [20] L. Sekaric, M. Zalalutdinov, R. B. Bhiladvala, A. T. Zehnder, J. Parpia, and H. G. Craighead, "Operation of nanomechanical resonant structures in air," *Applied Physics Letters*, vol. 81, pp. 2641–2643, 2002.
- [21] L. Sekaric, "Studies in nems: Nanoscale dynamics, energy dissipation, and structural materials," Ph.D. dissertation, Cornell University, 2003.
- [22] M. Zalalutdinov, A. Olkhovets, A. T. Zehnder, B. Ilic, D. Czaplewski, H. G. Craighead, and J. M. Parpia, "Optically pumped parametric amplification for micromechanical oscillators," *Applied Physics Letters*, vol. 78, pp. 3142–3144, 2001.
- [23] M. Zalalutdinov, K. Aubin, M. Pandey, A. Zehnder, R. Rand, B. Houston, J. Parpia, and H. Craighead, "Frequency entrainment for micromechanical oscillator," *Applied Physics Letters*, vol. 83, pp. 3281–3283, 2003.
- [24] D. Carr and H. G. Craighead, "Fabrication of nanoelectromechanical systems in single crystal silicon using silicon on insulator substrates and electron beam lithography," *Journal of Vacuum Science and Technology*, vol. B 15, pp. 2760–2763, 1997.
- [25] D. Carr, L. Sekaric, and H. G. Craighead, "Measurement of nanomechanical resonant structures in single-crystal silicon," *Journal of Vacuum Science and Technology*, vol. B 16, pp. 3281–3285, 1998.

- [26] K. Aubin, M. Zalalutdinov, R. Reichenbach, B. Houston, A. T. Zehnder, J. M. Parpia, and H. G. Craighead, "Laser annealing for high-q mems resonators," in *Microtechnologies for the New Millenium*. SPIE, 2003.
- [27] Z. Knittel, *Optics of Thin Films*. Wiley, 1976.
- [28] B. H. Billings, *American Institute of Physics Handbook*. McGraw-Hill, 1982, ch. 6.
- [29] S. Timoshenko, D. H. Young, and J. W. Weaver, *Vibration Problems in Engineering*, 4th ed. John Wiley & Sons, 1974.
- [30] M. Zalalutdinov, J. Parpia, K. Aubin, H. Craighead, T. Alan, A. Zehnder, and R. Rand, "Hopf bifurcation in a disk-shaped nems," in *Proceedings of the 2003 ASME Design Engineering Technical Conference*. American Society of Mechanical Engineers, 2003.
- [31] N. Ono, K. Kitamura, K. Nakajima, and Y. Shimanuki, "Measurement of Young's modulus of silicon single crystal at high temperature and its dependence of boron concentration using the flexural vibration method," *Japan Journal of Applied Physics*, vol. 39, pp. 368–371, 2000.
- [32] R. J. Pitcher, K. W. H. Foulds, J. A. Clements, and J. M. Naden, "Optothermal drive os silicon resonators: The influence of surface coatings," *Sensors and Actuators A*, vol. 21-23, pp. 387–390, 1990.
- [33] R. M. A. Fatah, "Mechanisms of optical activation of micromechanical resonators," *Sensors and Actuators A*, vol. 33, pp. 229–236, 1992.
- [34] S. Baglio, S. Castorina, L. Fortuna, and N. Savalli, "Modeling and design of novel photo-thermal-mechanical microactuators," *Sensors and Actuators A*, vol. 101, pp. 185–193, 2002.
- [35] R. G. Stearns and G. S. Kino, "Effect of electronic strain on photoacoustic generation in silicon," *Applied Physics Letters*, vol. 47, pp. 1048–1050, 1985.
- [36] A. Prak and T. S. J. Lammerink, "Effect of electronic strain on the optically induced mechanical moment in silicon microstructures," *Journal of Applied Physics*, vol. 71, pp. 5242–5245, 1992.
- [37] P. G. Datskos, S. Rajic, and I. Datskou, "Photoinduced and thermal stress in silicon microcantilevers," *Applied Physics Letters*, vol. 73, pp. 2319–2321, 1998.
- [38] —, "Detection of infrared photons using the electronic stress in metal-semiconductor cantilever interfaces," *Ultramicroscopy*, vol. 82, pp. 49–56, 2000.